PAPER

Check for updates

Preparation of F-doped $H_2Ti_3O_7$-{104} nanorods with oxygen vacancies using $TiOF_2$ as precursor and its photocatalytic degradation activity

Yue Jian,[ac] Huayang Liu,[b] Jiaming Zhu,[ac] Yaqiong Zeng,[ac] Zuohua Liu,[a] Chentao Hou [ID] *[b] and Shihua Pu*[ac]

Photocatalytic degradation is an eco-friendly and sustainable method for the treatment of water pollutants especially tetracycline hydrochloride (TCH). Herein, we developed F-doped $H_2Ti_3O_7$-{104} nanorods with oxygen vacancies using $TiOF_2$ as a precursor by simple alkali hydrothermal and ion-exchange methods. The phase structure, surface composition, optical properties, specific surface areas and charge separation were analysed by a series of measurements. The effects of KOH concentration on the structure and properties of $H_2Ti_3O_7$ were investigated. It is confirmed that the $TiOF_2/H_2Ti_3O_7$ composite can be formed in low concentration KOH solution (1 mol L^{-1}), while the $H_2Ti_3O_7$ single phase can be formed in high concentration KOH solution (>3 mol L^{-1}). The prepared F-doped $H_2Ti_3O_7$-{104} nanorods provide a high specific surface area of 457 m^2 g^{-1} and a macroporous volume of 0.69 cm^3 g^{-1}. The appropriate mesoporous structure of the photocatalyst makes TCH have a stronger affinity on its surface, which is more conducive to the subsequent photodegradation. Moreover, a synergistic mechanism of photosensitization and ligand−metal charge transfer (LMCT) in the photocatalytic degradation of TCH was proposed. In addition, the prepared F-doped $H_2Ti_3O_7$-{104} nanorods showed excellent cycle stability and resistance to light corrosion. After five cycles of photodegradation, the degradation rate of TCH was only reduced from 92% to 83%. This low-cost strategy could be used for the mass production of efficient photocatalysts, which can be used for TCH clean-up in wastewater treatment.

1. Introduction

With the widespread use of antibiotics, they have become a new pollutant in the water environment in recent years. It is particularly worth mentioning that more than dozens of sulfonamides, tetracyclines, and fluoroquinolone antibiotics have been detected in surface water and groundwater.[1,2] Their presence in the aquatic system enhances bacterial resistance, thereby inhibiting the effectiveness of common antibiotics in the treatment of microbial infections.[3–5]

Tetracycline hydrochloride (TCH) is a typical tetracycline broad-spectrum antibiotic, which is widely used as a growth promoter in the treatment of human diseases and animal feeding.[6] However, TCH is not easily degraded in the environment and poses a huge threat to the ecological environment, aquatic plants, animals, and human health.[7,8] In order to solve these problems, many advanced technologies have emerged in

the field of TCH degradation, such as adsorption,[9] biodegradation,[10] electrochemical oxidation,[11] membrane filtration,[12] and photocatalytic degradation.[13] Among them photocatalytic degradation is the most advantageous method to remove total organic carbon because of its low cost, strong oxidizing ability, and being eco-friendly. However, whether the photocatalytic technology can successfully achieve high-efficiency removal of pollutants in the water environment depends on the mineralization capacity and catalytic activity of the photocatalyst.[14,15] Therefore, the design and synthesis of photocatalysts with excellent mineralization ability and efficient charge separation are of great value to the photodegradation of TCH in water environments.

Hydrogen trititanate ($H_2Ti_3O_7$), as a new type of titanium-based semiconductor material, has attracted great interest due to its exciting characteristics, such as high specific surface area, high photo-reactivity and non-toxicity. Nowadays, $H_2Ti_3O_7$ has been used by some researchers for water decomposition,[16] CO_2 adsorption,[17] supercapacitors,[18] and photocatalytic degradation of organic pollutants.[19–21] However, a pure $H_2Ti_3O_7$ only responds to ultraviolet light, and due to the rapid combination of carriers after excitation, the photocatalytic degradation of organic pollutants is not satisfactory.

In recent years, people have conducted a lot of research on improving the photocatalytic activity of $H_2Ti_3O_7$. High

[a]Chongqing Academy of Animal Sciences, Chongqing 402460, China. E-mail: pu88962@126.com

[b]College of Geology and Environment, Xi'an University of Science and Technology, Xi'an 710054, China. E-mail: 807484470@qq.com

[c]Scientific Observation and Experiment Station of Livestock Equipment Engineering in Southwest, Ministry of Agriculture and Rural Affairs, Chongqing 402460, China

temperature heat treatment, non-metal doping (such as carbon, nitrogen and fluorine) and metal doping/deposition (including transition metals and precious metals) are widely used.[22,23] In particular, the doping of foreign elements plays a key role in the transient capture of photo-induced electrons and holes, which may be beneficial to inhibit the recombination of photogenerated charge carriers. Non-metallic doping is favored by researchers because of its low cost and simple operation. Fluorine doping can usually generate oxygen vacancies in titanium-based semiconductors by forming Ti–F–Ti bonds.[24] The appearance of Ti^{3+} is usually accompanied by oxygen vacancies.[25] This effectively reduces the recombination of carriers. It is worth noting that the remaining unsaturated Ti(VI) atoms may form an electronic coupling with the π orbital connected to –OH in TCH to form a complex of $H_2Ti_3O_7$ and tetracycline hydrochloride.[26,27] The strong ligand–metal charge transfer (LMCT) and photosensitization enhance $H_2Ti_3O_7$ response to visible light.

Nowadays, the most common method is to synthesize $Na_2Ti_3O_7$ by alkaline hydrothermal method with Ti-based material as the precursor and NaOH as the promoter, and then obtain $H_2Ti_3O_7$ by the H^+ exchange method. The reaction conditions play a crucial role in controlling the morphology and size of the $H_2Ti_3O_7$ nanostructures. For instance, Chang et al.[28] synthesized $H_2Ti_3O_7$ nanowires directly on titanium foil through a simple alkaline hydrothermal and ion-exchange process. Xiao et al.[29] prepared $H_2Ti_3O_7$ nanobelts by alkaline hydrothermal and HCl ion-exchange with Degussa P25 as precursor and NaOH as stripping agent. However, most of the synthesized $H_2Ti_3O_7$ has exposed {020}, {202}, {200} crystal planes, and almost few research has synthesized $H_2Ti_3O_7$ with {104} crystal plane exposed. $TiOF_2$ is a metastable phase, and they often appear as intermediates in the preparation of TiO_2 with exposed {001} planes.[30,31] Interestingly, $TiOF_2$ can be transformed into F-doped TiO_2 under certain hydrothermal conditions.[32–35] Therefore, it is possible to synthesize $K_2Ti_3O_7$ under alkaline hydrothermal conditions with $TiOF_2$ as the source of titanium and fluorine, and KOH as the promoter. Through simple HCl ion-exchange, $K_2Ti_3O_7$ is further transformed into F-doped $H_2Ti_3O_7$ nanorods with oxygen vacancies. As far as we know, few people use $TiOF_2$ as a precursor to synthesize $H_2Ti_3O_7$ nanorods.

Herein, we reported a method to synthesize F-doped $H_2Ti_3O_7$-{104} nanorods with oxygen vacancies by alkaline hydrothermal method and ion exchange method using cubic $TiOF_2$ as the precursor KOH as the promoter. The mechanism of synergistic effect of LMCT and photosensitization on the degradation of TCH by $H_2Ti_3O_7$ nanorods was proposed. This study provides a new idea for the preparation of $H_2Ti_3O_7$ photocatalyst and the degradation of TCH.

2. Experimental section

2.1. Chemicals

Tetrabutyl titanate (TBOT, A. R.), potassium hydroxide (KOH, A. R.), benzoquinone (BQ), methanol (MT), tert-butyl alcohol (t-BuOH), hydrochloric acid (HCl, A. R. 38%), glacial acetic acid

(CH₃COOH, A. R.), hydrofluoric acid (HF, A. R.) were purchased from Fuchen Chemical Reagent Factory, Tianjin, China. Tetracycline hydrochloride (TCH, A. R.) were purchased from Aladdin Industrial Corporation (Shanghai, China). Ultrapure water was used as experimental water.

2.2. Preparation of samples

$TiOF_2$ photocatalyst was synthesized by a simple one-step hydrothermal method using TBOT as titanium source. 40 mL of CH_3COOH and 20 mL of TBOT were added into 100 mL beaker, stir for 15 min at 26 °C, and obtained mixture was recorded as A. Next, 8 mL of HF was added to A with uniform stirring speed, and then the mixture was stirred at 26 °C for 1 h (HF has strong corrosivity, so attention should be paid to protection when taking it). Following that, the mixture was transferred into the polytetrafluoroethylene and placed in an autoclave and heated at 180 °C for 5 h. The products were collected by high-speed centrifugation and washed with ultrapure water and absolute ethanol for four times. Following that, dried at 60 °C and named $TiOF_2$.

F-doped $H_2Ti_3O_7$-{104} nanorods were synthesized by the alkali hydrothermal method and ion-exchange method using $TiOF_2$ as a precursor, KOH as stripping agent, and HCl as an ion exchanger. 0.5 g of $TiOF_2$ was mixed with 50 mL 10 M KOH aqueous solution in a 100 mL polytetrafluoroethylene liner stir at 25 °C for 1 h. Then, the polytetrafluoroethylene was placed in a high-pressure reactor and reacted at 150 °C for 4 h. After that, it was cooled to 25 °C, and the product was washed several times with 0.5 M HCl until the pH value of the filtrate become less than 7. Finally, the product was washed with ethanol and ultrapure water until the pH value of the filtrate reach to neutral. Following, the sample was dried at 60 °C and named 10 M-$TiOF_2$. The above process remained unchanged, except adding 1 M, 3 M, 5 M, and 15 M concentrations of KOH respectively and the obtained photocatalysts were named as 1 M-$TiOF_2$, 3 M-$TiOF_2$, 5 M-$TiOF_2$ and 15 M-$TiOF_2$.

To study the interaction mechanism between 10 M-$TiOF_2$ and TCH, the complex of 10 M-$TiOF_2$ and TCH were prepared. 10 M-$TiOF_2$ (20 mg) place into 100 mL TCH (20 mg L^{-1}), stirred for 60 min under dark conditions, and then froze and dried at −45 °C by vacuum freeze drier (Beijing Boyikang Scientific Instrument Co., Ltd). The obtained samples were recorded as 10 M-$TiOF_2$/TCH.

2.3. Characterization of the samples

The crystallinity of samples were confirmed by the Powder X-ray diffraction (XRD; Bruker D8 Advance X-ray diffractometer) at 36 kV, 20 mA equipped with a Cu anode X-ray tube (Cu Kα 1 X-rays, $\lambda = 1.54056$ Å). The morphology and structure of the samples were analysed by scanning electron microscope (SEM, JSM7500F, Japan) and transmission electron microscopic (TEM, JEOL JEM-2100 operated at 200 kV). The distribution of elements in the samples were analysed by energy dispersive spectrometer (EDS) setting on SEM. The N_2 adsorption/desorption isotherms of the samples were measured by Micromeritics JW-BK122W. The pore size distribution and specific

surface area of the samples were analysed by the Brunauer–Emmett–Teller (BET) and Barrett–Joyner–Halenda (BJH) methods at −196 °C. The chemical bonds and surface functional groups of samples were measured by Fourier transform infrared spectroscopy (FTIR, Nicolet IS5 Spectrometer, USA). The Ultraviolet-visible (UV-Vis) diffuse reflectance spectroscopy (DRS) of the samples were measured by UV-Vis spectrophotometer (Shimadzu Japan). The photoluminescence spectrum (PL) was acquired by a fluorescence spectrophotometer (Shimadzu-RF-6000, Japan). The chemical states of the elements in the samples were determined by X-ray photoelectron spectroscopy (XPS, Thermo SCIENTIFIC ESCALAB). The electron paramagnetic resonance (EPR) was recorded by Bruker 300 EPR electron paramagnetic resonance spectrometer.

2.4. Photocatalytic experiment

In order to know the degradation of TCH by the prepared material, 20 mg photocatalyst was dispersed into a quartz reaction tube containing 100 mL TCH (20 mg L^{-1}). The quartz tube stirred magnetically for 30 min. After the reaction system reached to the equilibrium of adsorption and desorption, the 500 W xenon lamp was turned on. Then, 7 mL of the mixture was taken out every 5 min, and the centrifuged liquid was used to determine the concentration of TCH. The concentration of TCH in the clarified solution was measured by ultraviolet visible spectrophotometer (L5S, Shanghai precision Instrument Co., Ltd) at the absorption wavelength of 357 nm. To measure the recyclability, the used 10 M-TiOF$_2$ was recycled after each photodegradation experiment as follows: the used 10 M-TiOF$_2$ was centrifuged, washed several times, and dried at 60 °C for next photodegradation. The dosage of sample was changed from 0.01 g to 0.15 g, 0.20 g and 0.25 g to explore the best dosage of photocatalyst for TCH degradation. The initial concentration of TCH was changed from 20 mg L^{-1} to 30 mg L^{-1}, 40 mg L^{-1}, and 50 mg L^{-1} to explore the effect of different TCH concentrations on photocatalytic degradation. The main active species ($^{\bullet}O_2^{-}$,

$^{\bullet}$OH, h^{+}) in photocatalytic degradation were explored by adding different scavenger agents (benzoquinone (BQ), *tert*-butyl alcohol (*t*-BuOH) and methanol (MT)) in the reaction system.

2.5. Photoelectrochemical measurements

Transient photocurrent experiments were measured by an Autolab (PGSTAT204, Netherlands) in a standard three-electrode system. The fabricated photocatalyst films as the working electrodes, a Pt plate electrode used as the reference electrode, an Ag/AgCl (saturated in KCl) applied as the reference electrode and 0.5 mol L^{-1} Na$_2$SO$_4$ was used as the electrolyte. The irradiation light source was a 500 W Xe lamp. The electrochemical impedance spectroscopy (EIS) tests were conducted in the same configuration. The frequency ranged from 10^{-1} to 10^5 Hz and the AC amplitude was adjusted to 5 mV. To prepare the working electrode, the photocatalyst (5 mg) and 5 wt% Nafion solution (80 μL) were dispersed in isopropyl alcohol (920 μL). Then, the mixture (100 μL) was drop casted on a 5 cm × 1 cm fluorine-doped tin oxide (FTO) glass electrode.

3. Results and discussion

3.1. Crystal structure of photocatalysts

Fig. 1 provides the XRD patterns of the samples. Fig. 1a clearly shows the crystal structure of the prepared TiOF$_2$. The diffraction peaks of the TiOF$_2$ are very sharp, which shows that the crystal of the material is good. Besides, the diffraction peaks at $2\theta = 23.68°, 33.50°, 48.14°, 54.18°, 60.13°,$ and $66.95°$ are attributed to the {100}, {110}, {200}, {210}, {211}, and {220} planes of cubic TiOF$_2$ (JCPDS no. 08-0060) indicating that the cubic TiOF$_2$ was successfully prepared.[24,34]
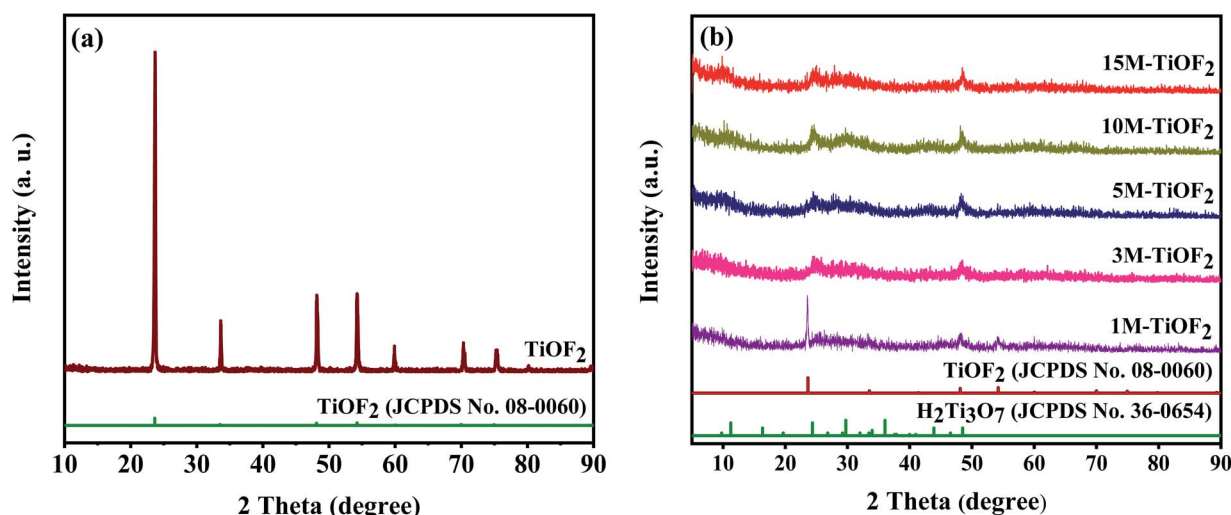
Fig. 1b shows the XRD patterns of the samples obtained from the TiOF$_2$ precursor after alkali hydrothermal and ion-exchange treatment. The diffraction peaks at $2\theta = 23.68°, 33.50°, 48.14°, 54.18°, 60.13°,$ and $66.95°$ are attributed to the {100}, {110}, {200}, {210}, {211}, and {220} planes of cubic TiOF$_2$ (JCPDS no.

Fig. 1 XRD patterns of TiOF$_2$ precursor (a) and samples obtained from the TiOF$_2$ precursor after alkali hydrothermal and ion-exchange treatment (b).

08-0060), and the diffraction peaks at $2\theta = 9.78°$, $11.25°$, $24.35°$, $29.73°$, $48.49°$ are attributed to the reflections of the {001}, {100}, {102}, {020} planes of $H_2Ti_3O_7$ (JCPDS no. 36-0654).[21] For 1 M-TiOF$_2$, it has two crystal phases of $TiOF_2$ and $H_2Ti_3O_7$ which indicates that in the presence of low concentration of KOH, a small part of $TiOF_2$ cannot be transformed into $K_2Ti_3O_7$, which cannot participate in the subsequent ion-exchange reaction, so $TiOF_2/H_2Ti_3O_7$ composite is formed. For 3 M-TiOF$_2$, 5 M-TiOF$_2$, 10 M-TiOF$_2$, and 15 M-TiOF$_2$, only $H_2Ti_3O_7$ crystal phase was formed. Therefore, pure $H_2Ti_3O_7$ photocatalyst could be successfully prepared from $TiOF_2$ precursor at high concentration of KOH. It is worth noting that 10 M-TiOF$_2$ and 15 M-TiOF$_2$ have good crystallinity, indicating that high concentration of KOH is conducive to crystallization.

3.2. Morphology analysis of samples

The morphology of all samples was further studied by scanning electron microscopy analysis. As shown in Fig. 2a, the $TiOF_2$ precursor consists of a mixture of cubic and spherical particles with an average size of 280–500 nm (which corresponds to the diameter of the sphere or the side of the cube). Compared with some other results of the prepared $TiOF_2$,[35–37] the morphology of the precursor obtained in this study is not uniform.

Fig. 2b–f show the images of the products obtained by alkaline hydrothermal and ion-exchange using $TiOF_2$ as a precursor with different mole of KOH. It can be seen that the morphology of the samples changed greatly after alkali treatment and ion-exchange. In the alkaline hydrothermal environment of 1 M KOH, the surface of $TiOF_2$ was etched and the cubic
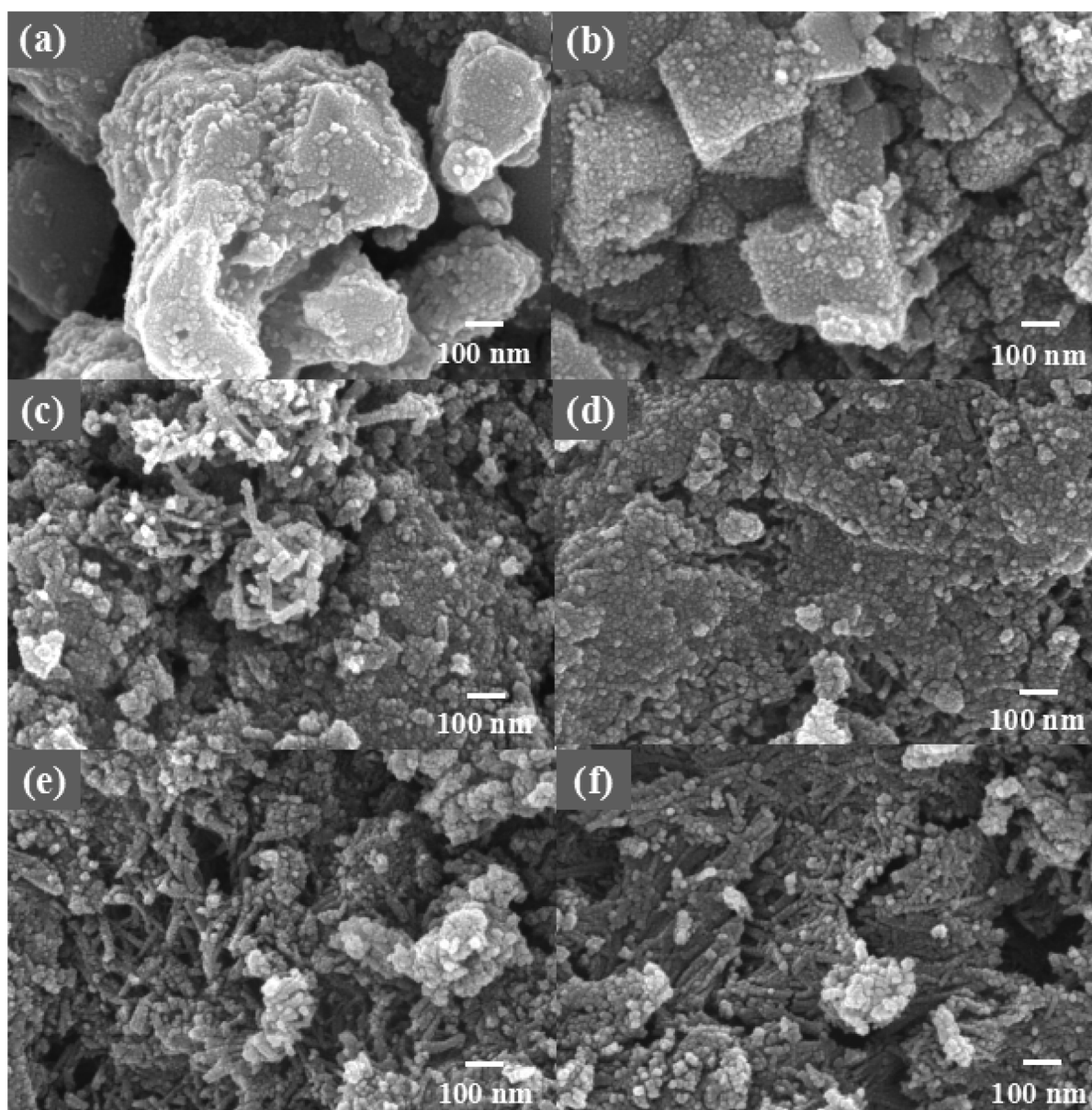

Fig. 2 SEM images of (a) TiOF$_2$, (b)1 M-TiOF$_2$, (c) 3 M-TiOF$_2$, (d) 5 M-TiOF$_2$, (e) 10 M-TiOF$_2$ and (f) 15 M-TiOF$_2$.

surface became rough (Fig. 2b). This is because part of the cubic $TiOF_2$ was stripped by KOH to form $K_2Ti_3O_7$, and then exchanged with H^+ to form a small part of $H_2Ti_3O_7$ single crystal particles with the size of 30–50 nm attached to the surface of the residual cubic $TiOF_2$. When the KOH is further increased to 3 M, the phase of $TiOF_2$ has completely transformed into $H_2Ti_3O_7$, and the cubic $TiOF_2$ precursor no longer exists (Fig. 2c). 3 M-$TiOF_2$ shows that the irregular $H_2Ti_3O_7$ particles with the size of 20–30 nm aggregate into blocks, and some $H_2Ti_3O_7$ particles aggregate into rods with the size of 50–100 nm. With the increase of KOH to 5 M, it can be seen that there are a lot of staggered $H_2Ti_3O_7$ nanorods in 5 M-$TiOF_2$, and some $H_2Ti_3O_7$ particles are aggregated into lamellar structure (Fig. 2d).

When the concentration of KOH is 10 M, $H_2Ti_3O_7$ nanorods are staggered with an average size of 40–70 nm, and a small part of $H_2Ti_3O_7$ is aggregated into irregular blocks with an average size of 200–300 nm (Fig. 2e). These nanorods assembled by $H_2Ti_3O_7$ particles have many reactive sites, and increase the contact area between $H_2Ti_3O_7$ and TCH, which makes TCH more easily adsorbed on its surface for photocatalytic degradation.[38] When the concentration of KOH is 15 M, $H_2Ti_3O_7$ nanorods with an average size of 70–150 nm tend to form. These nanorods are more aggregated, and the pore ratio is less than 10 M-$TiOF_2$ (Fig. 2f).

To further study the morphological features of the 10 M-$TiOF_2$, TEM, HRTEM, and EDS images of prepared 10 M-$TiOF_2$

are shown in Fig. 3. It can be seen from Fig. 3a that 10 M-$TiOF_2$ is composed of nanorods with an average size of 40–70 nm, which is consistent with the results of SEM observation. In Fig. 3b, the HRTEM image of 10 M-$TiOF_2$ nanorods shows a crystal plane spacing of 2.06 nm, which corresponds to the {104} crystal plane of $H_2Ti_3O_7$. Comparison In order to further describe the element distribution of 10 M-$TiOF_2$, an element mapping analysis was performed on 10 M-$TiOF_2$ (Fig. 3c–e). Ti, O, and F are evenly distributed. These results confirm that we have successfully synthesized F-doped $H_2Ti_3O_7$-{104} nanorods.

3.3. BET specific surface area and pore structure

The specific surface area and pore size distribution of $TiOF_2$ and 10 M-$TiOF_2$ were analysed by nitrogen adsorption–desorption technology. As shown in Fig. 4a, according to the classification of IUPAC, $TiOF_2$ shows a typical IV type adsorption desorption isotherm with H4 type hysteresis ring, which represents that the sample has mesopore formation and matches the image presented by Fig. 2a. It can be seen from Fig. 4a inset of BJH pore size distribution diagram that the curves of the $TiOF_2$ are sharp, and the pore size distribution is mainly 2–8 nm, which indicates that there is a uniform pore size distribution in catalyst. As shown in Fig. 4b, 10 M-$TiOF_2$ exhibit an IV shape of isotherm and an H2b shape hysteresis loop, indicating that there are pipe-shaped pores with uneven pore size distribution and interstitial pores of close-packed spherical particles in the 10 M-
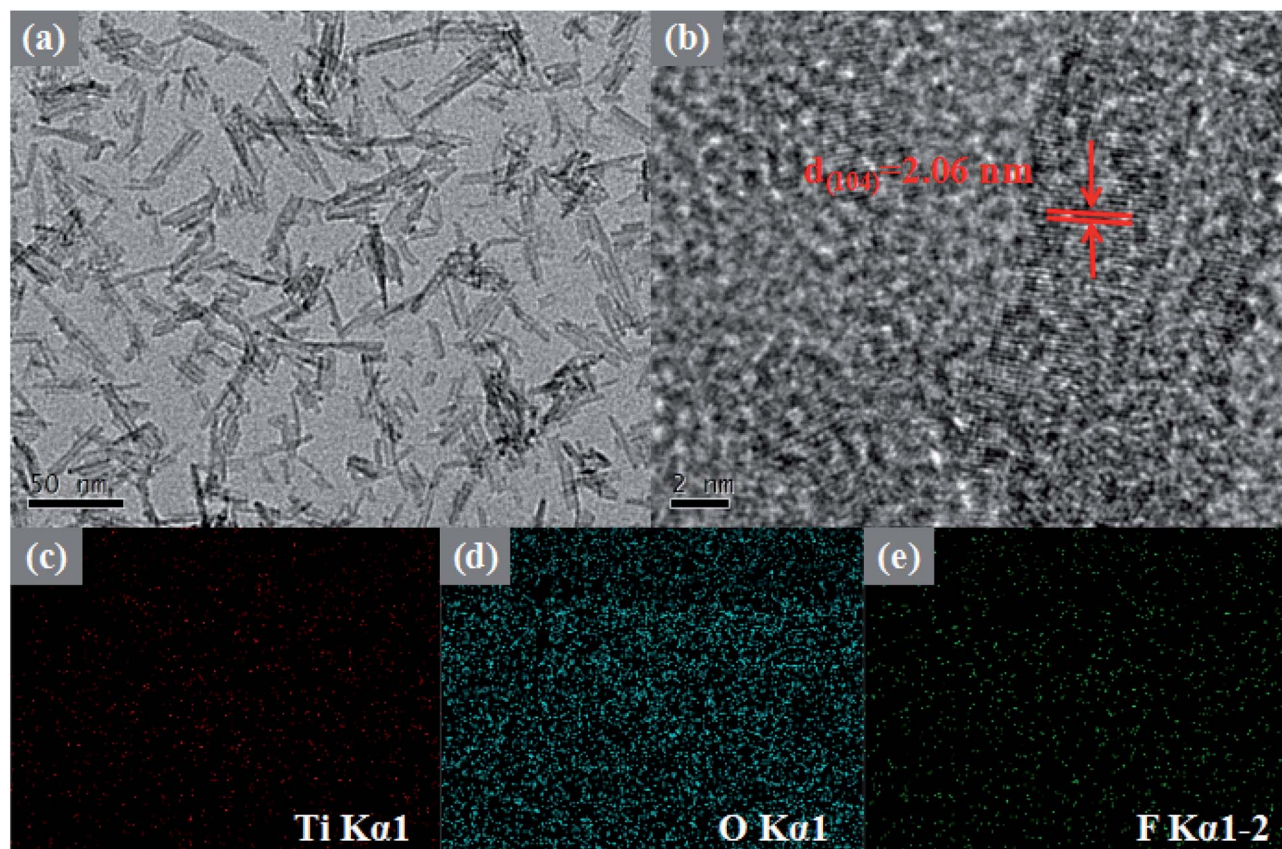

Fig. 3 TEM and HRTEM images of 10 M-$TiOF_2$ (a and b); elemental mapping of 8-TF (c−e).
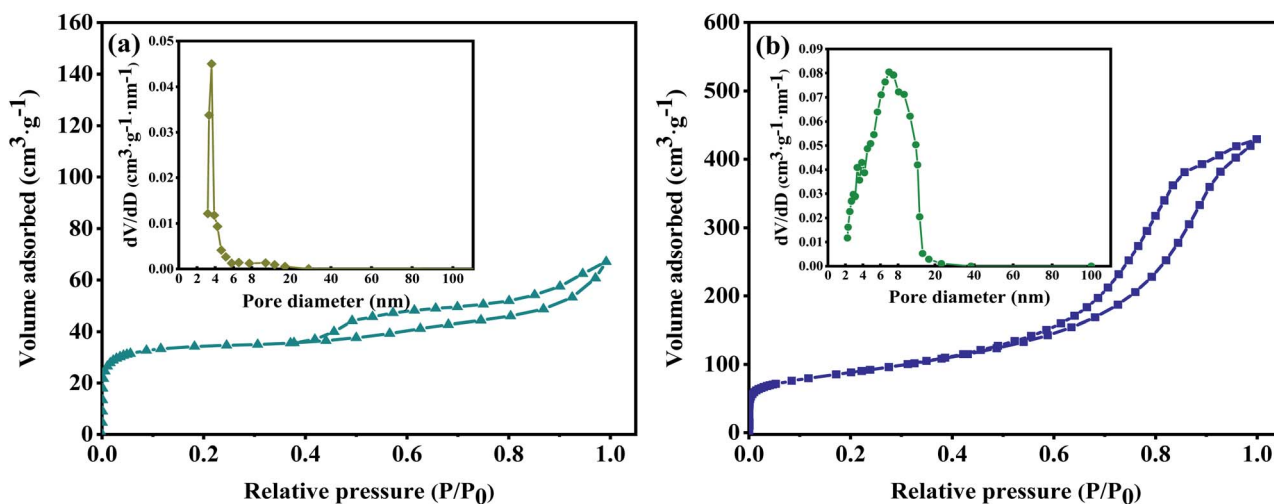
Fig. 4 Nitrogen adsorption–desorption isotherms of $TiOF_2$ (a) and 10 M-$TiOF_2$ (b). The inset shows the corresponding pore size distribution of $TiOF_2$ and 10 M-$TiOF_2$.

$TiOF_2$, which is consistent with the results observed in Fig. 2e. The pore size of 10 M-$TiOF_2$ is mostly concentrated in 2–20 nm (the inset of Fig. 4b), which indicates that $H_2Ti_3O_7$ nanorods have ordered mesoporous structure.

The presence of mesopores favours multilight scattering, resulting in enhanced harvesting of the exciting light and thus improved photocatalytic activity.[39,40] In addition, larger mesopores facilitates faster mass transport, resulting in improved performance.[41–48]

Table 1 shows the specific surface area, pore volume, and average pore size for the tested samples. It can be seen that the specific surface area of 10 M-$TiOF_2$ (457 m^2 g^{-1}) is about 114 times that of $TiOF_2$ (5 m^2 g^{-1}). After alkali hydrothermal and ion exchange treatment, the specific surface area and pore volume of 10 M-$TiOF_2$ were greatly increased compared with $TiOF_2$. This indicates that alkali hydrothermal treatment can effectively increase the surface area of the catalyst, which is consistent with the research of Teng et al.[49] 10 M-$TiOF_2$ showed a high specific surface area of 457 m^2 g^{-1} and pore volume of 0.69 cm^3 g^{-1} which made the TCH adsorb on the surface of the catalyst rapidly. The unsaturated Ti^{4+} in $H_2Ti_3O_7$ and the delocalized π bond with –OH group in TCH rapidly form ligand to metal charge transfer (LMCT), which greatly improves the response of visible light.[50] This is confirmed by the subsequent UV-Vis absorbance spectra.

3.4. FT-IR analysis

The chemical functional groups of the samples were analysed by FT-IR Fig. 5. The peak at 3260 cm^{-1} corresponds to the O–H stretching vibration of adsorbed water.[51] The peak at 1628 cm^{-1} corresponds to the bending vibration of Ti–OH, which is attributed to the formation of –OH on the surface of catalysts by hydrothermal process.[52] The peak at 534 cm^{-1} can be corresponded to the Ti–O vibration in $TiOF_2$.[53] It should be noted that the peak of 1 M-$TiOF_2$, 3 M-$TiOF_2$, 5 M-$TiOF_2$, 10 M-$TiOF_2$ and 15 M-$TiOF_2$ shifts negatively from 534 cm^{-1} which may be attributed to the increasing number of O_v in the lattice structure changes the number of Ti atom surrounding the O atom, and the electron cloud density around a Ti atom decreased.[24] This was confirmed by EPR and XPS. It can be seen that there are peaks at 922 cm^{-1} in all samples which is attributed to the
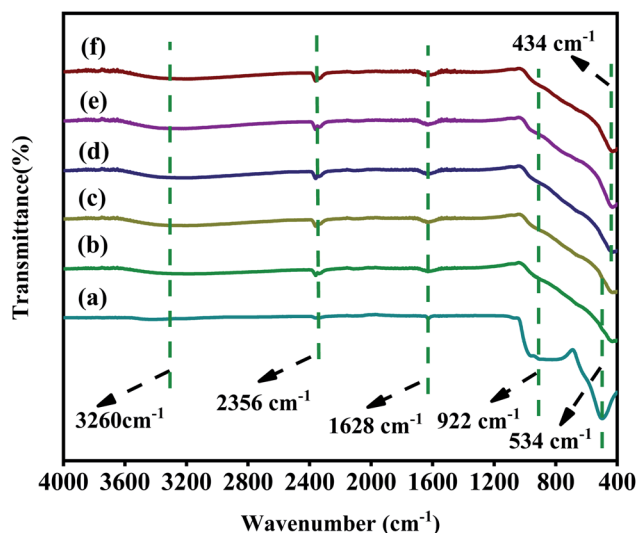
Table 1 Specific surface area, pore volume, and average pore size of $TiOF_2$ and 10 M-$TiOF_2$

Samples	Surface area (m^2 g^{-1})	Pore volume (cm^3 g^{-1})	Average pore size (nm)
$TiOF_2$	4	0.02	9.02
10 M-$TiOF_2$	457	0.69	7.76

Fig. 5 FT-IR spectra of samples: (a) $TiOF_2$, (b) 1 M-$TiOF_2$, (c) 3 M-$TiOF_2$, (d) 5 M-$TiOF_2$, (e) 10 M-$TiOF_2$ and (f) 15 M-$TiOF_2$.

existence of the Ti–F bond.[54] Besides, the peak at 2356 cm^{-1} corresponds to the absorbed CO_2.

3.5. Electronic states of photocatalyst

The survey XPS spectra showed Ti, O, C, and F elements in the 10 M-TiOF$_2$ (Fig. 6a). The CO_2 absorbed by the pore structure of the sample leads to the existence of C.[55,56] Two diffraction peaks at 458.7 and 464.5 eV in the high-resolution spectrum of Ti 2p (Fig. 6b) corresponds to Ti 2p$_{3/2}$ and Ti 2p$_{1/2}$, respectively. The signals at 458.8 and 464.9 eV can correspond to Ti^{4+} 2p$_{3/2}$ and Ti^{4+} 2p$_{1/2}$, and the distance between the two signal peaks is 5.7 eV, which is strong evidence for the existence of Ti^{4+}, indicating that a part of Ti in 10 M-TiOF$_2$ exists in the form of Ti^{4+}.[57,58] The signal peaks at 458.4 and 463.8 eV can be attributed to the presence of Ti^{3+} 2p$_{3/2}$ and Ti^{3+} 2p$_{1/2}$ in the catalyst. The distance between signal peaks confirmed that a part of Ti existed in the form of Ti^{3+}.[33,59]

The states of O in the 10 M-TiOF$_2$ were further studied. The spectrum of O 1s orbital is shown in Fig. 6c. The signal peaks at 530.1, 530.5, 531.4, and 532.2 eV is corresponding to the lattice oxygen (Ti–O), hydroxyl oxygen (Ti–OH), oxygen vacancies (O$_v$) associated with Ti^{3+}, and oxygen in adsorbed water in the catalyst. This indicates that the photocatalyst contains high concentration of Ti^{3+}/O$_v$. It has been proved in the previous research that oxygen defects are more easily compatible with water molecules in the air and can be further converted into hydroxyl groups, which is consistent with the results of FT-IR. The existence of Ti^{3+}/O$_v$ species in TiOF$_2$ and 10 M-TiOF$_2$ was further confirmed by EPR analysis (Fig. 6d). A strong electron paramagnetic signal was observed at $g = 2.002$, which can be attributed to the existence of single electron O$_v$ induced by Ti^{3+} in 10 M-TiOF$_2$. It is well known that the surface O$_v$ associated with Ti^{3+} is extremely unstable in water or air because it is easily oxidized to O$_2^-$.[60] However, no signal of surface Ti^{3+} species ($g = 2.02$) was observed in EPR spectra. Therefore, Ti^{3+}/O$_v$ species exist inside the catalyst rather than on the surface, which makes it stable in air or aqueous solution.
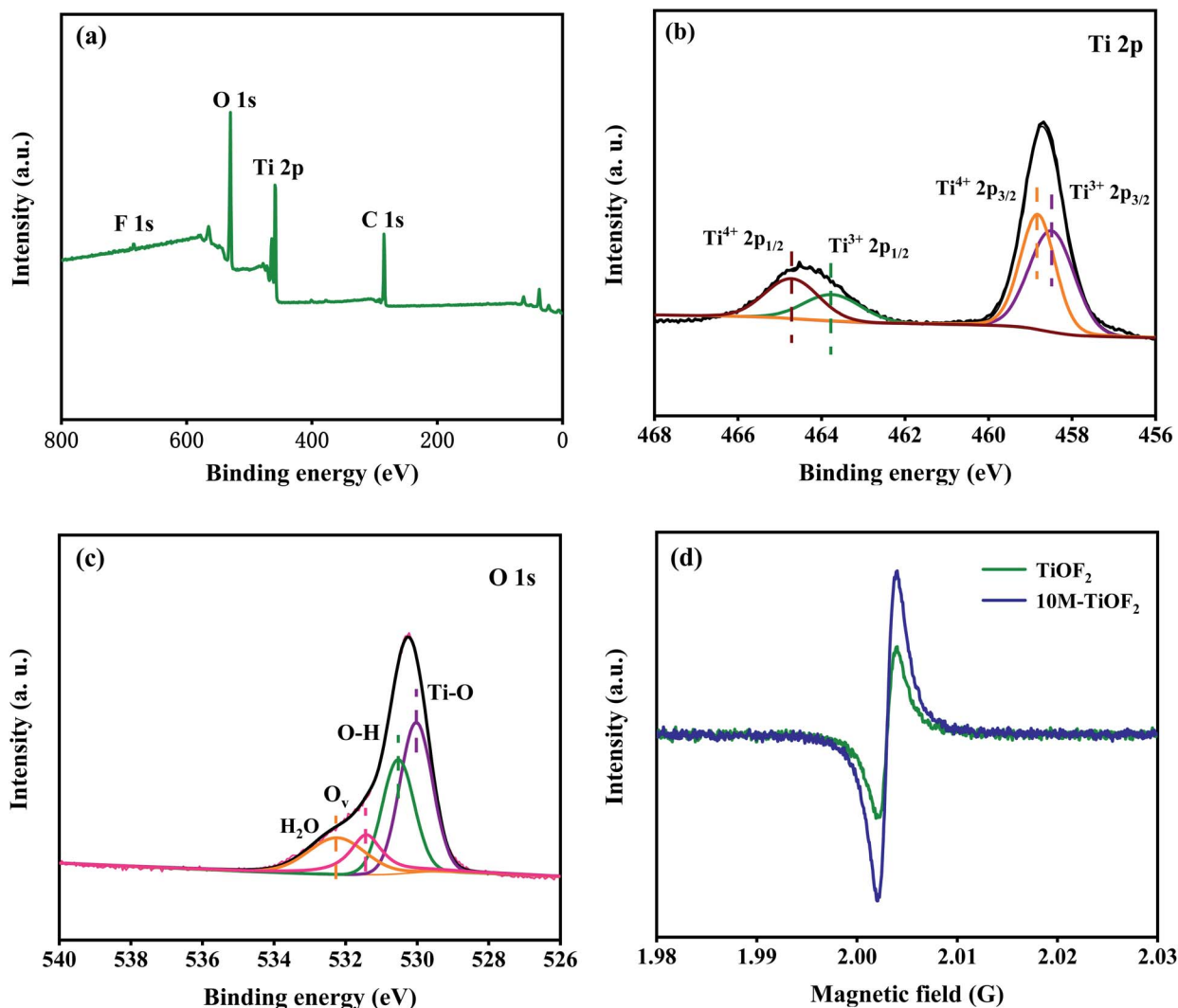

Fig. 6 High-resolution XPS spectra XPS spectra of as-prepared 10 M-TiOF$_2$: (a) survey spectra. (b) Ti 2p, (c) O 1s; (d) EPR spectra of TiOF$_2$ and 10 M-TiOF$_2$.

3.6. Optical performance analysis

The optical absorption properties of the samples were analysed by UV-Vis-DRS. Fig. 7a shows the light absorption properties of TCH, different photocatalysts, and their complex. In the absence of TCH adsorption, all photocatalysts have strong absorption for the light with a wavelength of less than 390 nm. The amount of light absorbed in the UV region increased in the order 3 M-TiOF$_2$ < TiOF$_2$ < 5 M-TiOF$_2$ < 15 M-TiOF$_2$ < 1 M-TiOF$_2$ < 10 M-TiOF$_2$. However, the photocatalysts exhibit weak absorption bands in the visible region. TCH molecule has a delocalized π bond with the –OH group, which leads to a small energy gap between the highest occupied molecular orbital (HOMO) and the lowest unoccupied molecular orbital (LUMO).[50] Therefore, TCH has a strong absorption band in the UV and visible regions. Interestingly, the complex of 10 M-TiOF$_2$ and TCH showed a stronger absorption band in the visible region than TCH. The complex of 10 M-TiOF$_2$ and TCH displayed the strongest absorption band in the visible region.

Most researchers believe that the ligand-to-metal charge transfer (LMCT) between TCH and coordinatively unsaturated Ti(IV) atom is the main reason for the new absorption band and redshift of the complex formed by TCH and Ti-based semiconductor (TiO$_2$ and TiOF$_2$).[24,61] H$_2$Ti$_3$O$_7$, as a Ti based semiconductor rich in unsaturated coordination Ti(IV), naturally has an LMCT mechanism with TCH. This may be an important reason for the broadening of the response region of the 10 M-TiOF$_2$/TCH to visible light. Besides, TCH adsorbed on H$_2$Ti$_3$O$_7$ but not interacted with Ti(IV) atom, due to its own visible light absorption characteristics, will be similar to the dye sensitization effect to promote the absorption of H$_2$Ti$_3$O$_7$ to visible light. The bandgap energy (E_g) of different photocatalysts was calculated according to the Tauc curve (Fig. 7b). The bandgap energies of TiOF$_2$, 1 M-TiOF$_2$, 3 M-TiOF$_2$, 5 M-TiOF$_2$, 10 M-TiOF$_2$, and 15 M-TiOF$_2$ are 2.97, 2.87, 2.97, 2.97, 2.96, and 2.98 eV. The narrow bandgap of 1 M-TiOF$_2$ may be due to the heterojunction formed by cubic TiOF$_2$ and H$_2$Ti$_3$O$_7$.

3.7. Charge separation properties

EIS is an effective technique to study interface charge separation and transfer.[62] The EIS Nyquist plots were performed to assess the conductivity of different samples. As shown in Fig. 8a, the semicircle diameter of TiOF$_2$ is larger than that of 10 M-TiOF$_2$, which indicates that 10 M-TiOF$_2$ has a lower electron transfer resistance. This may be because the band gap of 10 M-TiOF$_2$ is larger than that of TiOF$_2$, resulting in a higher carrier recombination degree than TiOF$_2$. The arc radius of 10 M-TiOF$_2$/TCH is smaller than that of TiOF$_2$ and 10 M-TiOF$_2$, indicating that photogenerated electrons of 10 M-TiOF$_2$/TCH transfer fastest. This might be due to the LMCT effect between 10 M-TiOF$_2$ and TCH, which makes the complex have smaller internal resistance and promotes the transfer efficiency of interface electrons. Moreover, under periodic sunlight, the photocurrent–time (I–t) curves of the synthesized TiOF$_2$, 10 M-TiOF$_2$, and 10 M-TiOF$_2$/TCH are shown in Fig. 8b. Obviously, the TiOF$_2$ and 10 M-TiOF$_2$ electrodes exhibit relatively low current intensity with a certain attenuation, which strongly reveals the internal recombination of light-induced charge carriers. When TCH is attached to the surface of 10 M-TiOF$_2$, the photocurrent intensity is significantly increased, which means that the LMCT mechanism formed when TCH is adsorbed on the surface of 10 M-TiOF$_2$ can effectively promote the rapid transfer of charge carriers, thereby enhancing the photocatalytic activity. This result is similar to that of Zhang et al.[61]

3.8. Photocatalytic performance

TCH is an extremely stable organic compound, which seldom self-degrades under light. Hence, the degradation of TCH must take place with the help of photocatalyst. This has been confirmed in previous studies.[4,10]

The adsorption degradation performance of different photocatalysts for TCH solution is shown in Fig. 9. It can be seen that different photocatalysts have reached adsorption–desorption equilibrium for TCH at 60 min. For TiOF$_2$, 1 M-TiOF$_2$, 3 M-
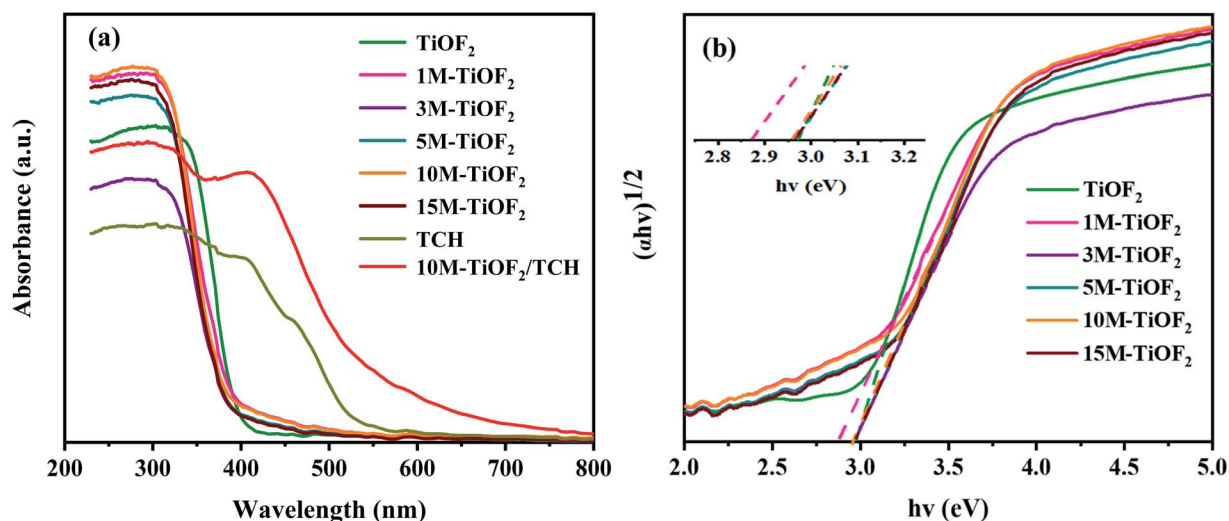

Fig. 7 (a) The UV-Vis DRS of prepared samples and (b) the curves of the $(\alpha h v)^{1/2}$ versus hv of prepared samples.
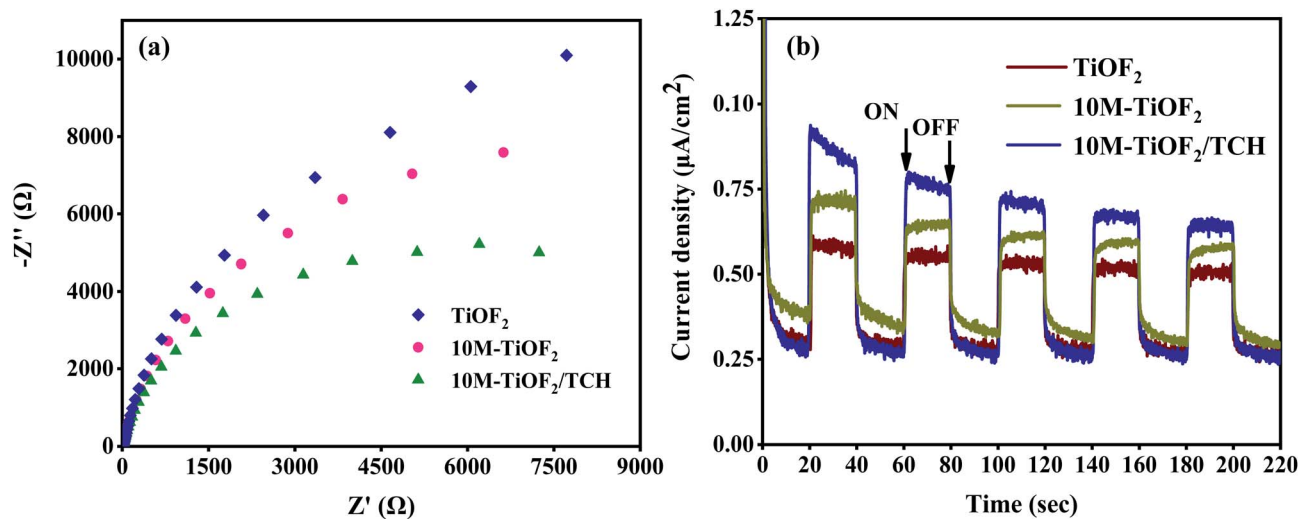
Fig. 8 (a) EIS Nyquist plots of TiOF$_2$, 10 M–TiOF$_2$ and 10 M–TiOF$_2$/TCH and (b) transient photocurrent responses of TiOF$_2$, 10 M–TiOF$_2$ and 10 M–TiOF$_2$/TCH.

TiOF$_2$, 5 M-TiOF$_2$, 10 M-TiOF$_2$, and 15 M-TiOF$_2$, when the adsorption–desorption reach equilibrium, the removal rates of TCH were 6%, 27%, 45%, 62%, 68%, and 65%, respectively.

The photocatalytic degradation performance of different photocatalysts for TCH solution is shown in Fig. 9a. Without the addition of photocatalyst, TCH almost has no self-degradation under simulated sunlight. After the simulated sunlight was turned on, the total removal rate of TCH by TiOF$_2$ was only 10%, which indicated that TiOF$_2$ showed the worst photocatalytic activity. Surprisingly, the removal rate of TCH by 10 M-TiOF$_2$ reached 88% only after 20 min illumination under simulated sunlight. After further illumination for 60 min, the total removal rate reached 92%. 1 M-TiOF$_2$, 3 M-TiOF$_2$, 5 M-TiOF$_2$, and 15 M-TiOF$_2$ also had higher removal rates of TCH, which were 56%, 88%, and 90%.

Furthermore, the exposure of {104} facets make H$_2$Ti$_3$O$_7$ have high reactivity, and the synergistic effect of LMCT and dye

sensitization enhances the visible light absorption of the photocatalyst. Fig. 10b shows the kinetic curves of photocatalysts. Typically, the variation of TCH concentration on irradiation time under simulated solar irradiation matches the pseudo first-order kinetic model.[63] The corresponding apparent rate constants k of TiOF$_2$, 1 M-TiOF$_2$, 3 M-TiOF$_2$, 5 M-TiOF$_2$, 10 M-TiOF$_2$, and 15 M-TiOF$_2$ were calculated to be 0.00156, 0.00811, 0.01711, 0.02026, 0.02285 and 0.02267 min^{-1}, respectively. The photocatalytic degradation rate of 10 M-TiOF$_2$ is about 15 times that of the TiOF$_2$.

The effects of different dosage of 10M-TiOF$_2$ (0.1 g L^{-1}, 0.2 g L^{-1}, 0.3 g L^{-1}, 0.4 g L^{-1}) on photocatalytic degradation of TCH were investigated (Fig. 10c). Photocatalyst was 0.1 g L^{-1}, the degradation efficiency was only 71%, which might be due to the fact that less photocatalyst is not enough to produce more active sites in the reaction system. When the dosage of 10M-TiOF$_2$ catalyst is 0.15 g L^{-1}, the degradation rate of TCH was 84%. Furthermore, the addition of 0.2 g L^{-1} and 0.25 g L^{-1} of catalyst can be as high as 92%. In addition, the effects of different concentrations of TCH solution on the photocatalytic performance of 10 M-TiOF$_2$ sample were studied (Fig. 10d). Obviously, 10 M-TiOF$_2$ had the best degradation effect on TCH solution of 20 mg L^{-1}. With the increase of TCH solution concentration, the photocatalytic performance of 10 M-TiOF$_2$ gradually decreased. It may be that the photocatalyst is not to provide enough active reaction sites to deal with so many TCH molecules.[24] Furthermore, the repeatability and sedimentation performance of the 10 M-TiOF$_2$ were evaluated. Fig. 11a shows the results of five consecutive cycles of photocatalytic degradation experiments. After five cycles, the degradation rate of 10 M-TiOF$_2$ decreased from 92% to 83%, indicating that 10 M-TiOF$_2$ has a high reuse rate. Fig. 11b shows the XRD pattern of 10 M-TiOF$_2$ after five cycles. The phase structure of the photocatalyst did not change obviously before and after the reaction, which indicated that the photocatalyst had good structural stability and reusability.
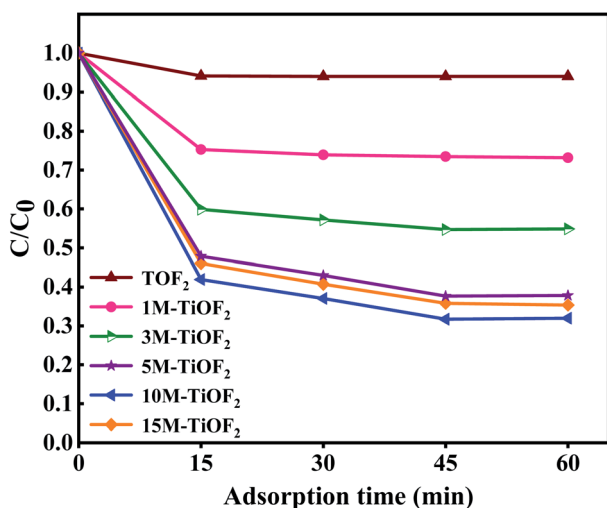

Fig. 9 Adsorption of TCH solution (20 mg L^{-1}, 100 mL) using different photocatalysts (0.2 g L^{-1}) in dark for 60 min.
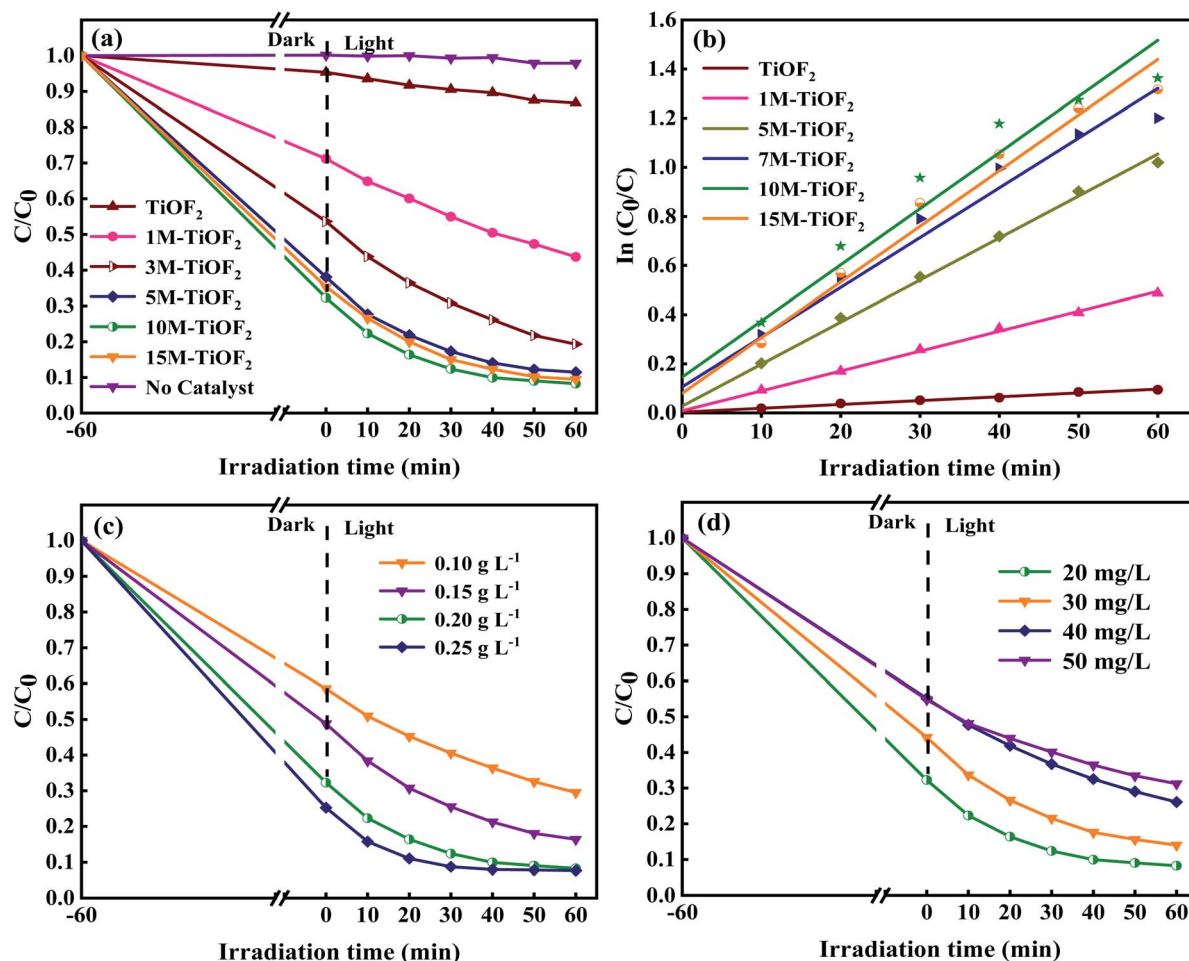
Fig. 10 (a) Photodegradation of TCH solution using different photocatalysts under simulated sunlight; (b) kinetics for as-prepared samples; (c) the effect of different dosage of 10 M-TiOF$_2$ on the degradation of TCH solution; (d) the effect of different concentration of TCH solution on the photocatalytic performance of 10 M-TiOF$_2$ under simulated sunlight.

3.9. Photocatalytic mechanism

Trapping tests were carried out to examine the photocatalytic mechanism of 10 M-TiOF$_2$ (Fig. 12). Scavengers such as BQ, MT, and *t*-BuOH were employed to capture $^{•}O_2^{-}$, h^{+}, and $^{•}$OH species, respectively.[6,37] The removal rate of TCH decreased from 92% to 69% when BQ was added into the system, which
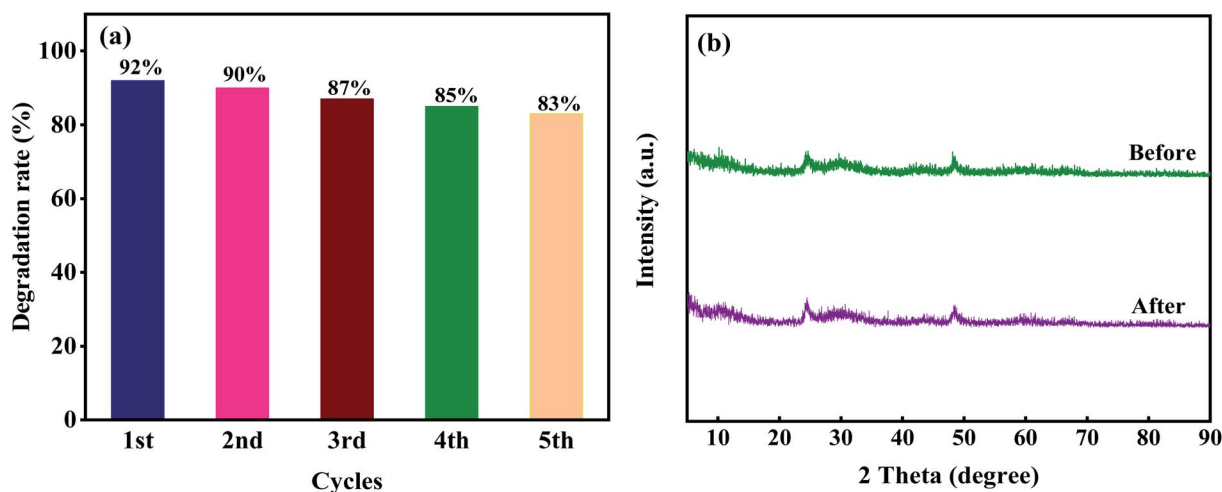

Fig. 11 (a) Stability tests over 10 M-TiOF$_2$ for TCH degradation; (b) XRD patterns of 10 M-TiOF$_2$ before and after five cycling runs.
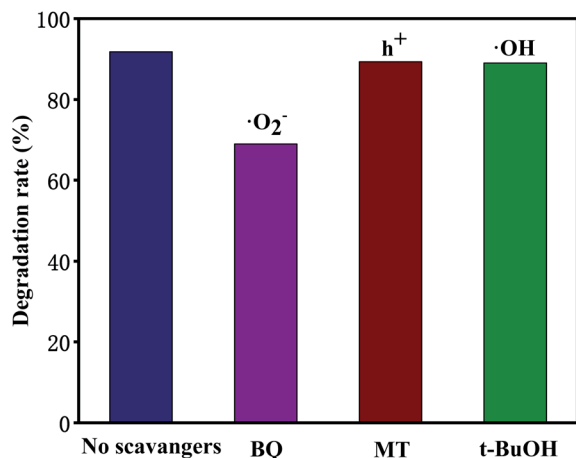
Fig. 12 Photocatalytic degradation rate of 10 M-TiOF$_2$ with the addition of different scavengers.

indicated that $\cdot O_2^-$ was the main active species in the degradation system. After adding MT and *t*-BuOH, the photocatalytic degradation was almost not inhibited, indicating that h$^+$ and $\cdot$OH did not play a major role in photodegradation.

As shown in Fig. 13, derived from the analysis presented above, we put forward the possible mechanism of degradation of TCH by 10 M-TiOF$_2$ under simulated sunlight. Firstly, the {104} facets of H$_2$Ti$_3$O$_7$ nanorods has a strong adsorption capacity for TCH. Furthermore, the π orbital of TCH may form electronic coupling with the 3d orbital of Ti^{4+}, resulting in a surface complex between TCH and H$_2$Ti$_3$O$_7$.[27] TCH was degraded simultaneously in two pathway. In the first path,

electrons are excited from HOMO level of TCH to LUMO level under simulated sunlight, and then rapidly injected into the conduction band (CB) position of H$_2$Ti$_3$O$_7$ facets.[24] However, TCH lost its electrons and remained a stable product (TCH$^+$). Such photoexcitation and injection process is often referred to as LMCT. In the second path, because of the limited number of unsaturated Ti(IV) atoms, the electrons of another part of uncoordinated TCH transition from the ground state (HOMO) to the excited state (LUMO), leaving a TCH$^+$ and further transfer to the conduction band of F-H$_2$Ti$_3$O$_7$ under the excitation of simulated sunlight. This process of light excitation and electron transfer is usually called dye sensitization. For F-H$_2$Ti$_3$O$_7$, Ti^{3+}/O$_v$ are widely distributed on the surface, which means that there are abundant traps on the surface. Due to the delocalization of electrons in the CB, the electrons transferred from TCH to F-H$_2$Ti$_3$O$_7$ CB and the electrons transferred from F-H$_2$Ti$_3$O$_7$ VB can easily migrate from F-H$_2$Ti$_3$O$_7$ CB to the surface trap, where they are trapped and stabilized.[64,65] Due to the CB potential, F-H$_2$Ti$_3$O$_7$ is more negative than that of O$_2$/$\cdot$O (-0.046 eV *vs.* NHE),[66] the adsorbed O$_2$ on the surface of the photocatalyst is more likely to capture the electrons and form $\cdot O_2^-$. These reactive superoxide radicals ($\cdot O_2^-$) can highly oxidize the TCH and TCH$^+$ into H$_2$O, CO$_2$, and some small molecules.

4. Conclusions

In summary, F-doped H$_2$Ti$_3$O$_7$-{104} nanorods with oxygen vacancies can be prepared by alkaline hydrothermal method combined with ion-exchange method using TiOF$_2$ as precursor. TiOF$_2$/H$_2$Ti$_3$O$_7$ composite can be formed in the low concentration KOH solution (1 mol L^{-1}), and H$_2$Ti$_3$O$_7$ single phase can be
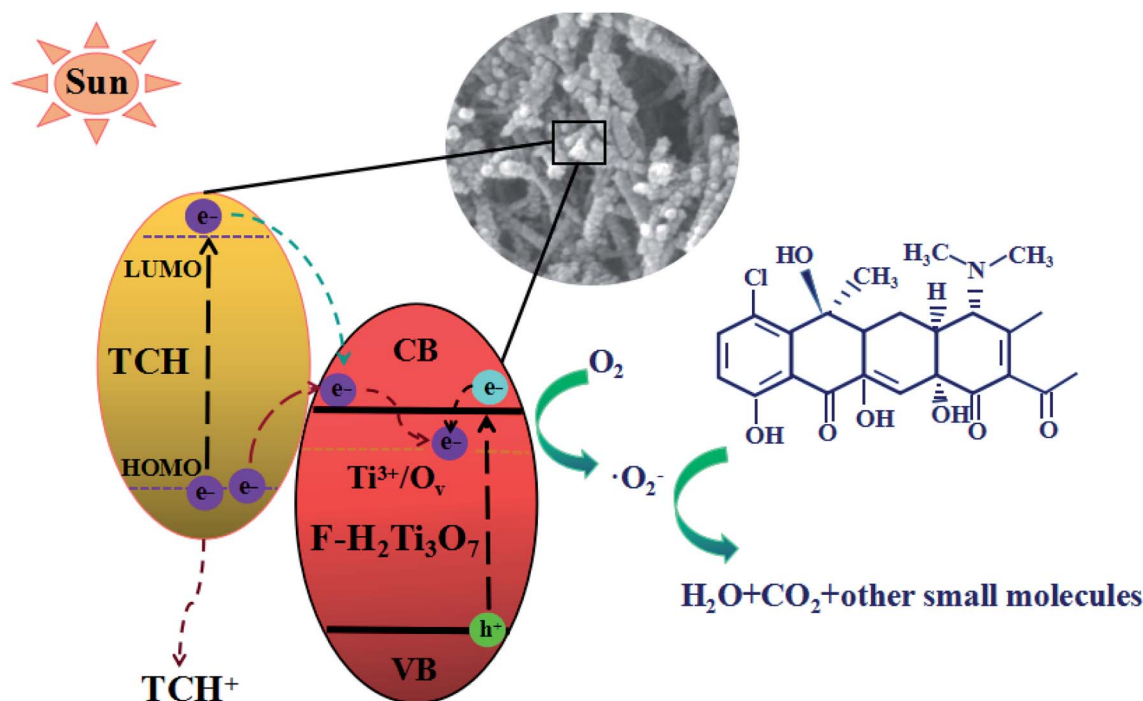

Fig. 13 Schematic shows the TCH degradation by 10 M-TiOF$_2$ photocatalyst.

formed in high concentration KOH solution (>3 mol L^{-1}). The synergy of LMCT effect between TCH and H$_2$Ti$_3$O$_7$ not only expands the visible light absorption region of H$_2$Ti$_3$O$_7$, but also improves the carrier separation ability. Thereby, it has excellent photocatalytic degradation performance for TCH. Furthermore, F-doped H$_2$Ti$_3$O$_7$-{104} nanorods stronger photochemical corrosion resistance. This simple and low-cost strategy can be used for large-scale production of photocatalysts, which is conducive to the practical application of wastewater purification process.

Conflicts of interest

The authors declare that they have no known competing financial interests or personal relationships that could have appeared to influence the work reported in this paper.

Acknowledgements

References

1 C. Hou and J. Hao, *RSC Adv.*, 2021, **11**, 26063–26072.

2 Z. Lin, S. Shen, Z. Wang and W. Zhong, *iScience*, 2021, **24**, 102469.

3 U. Ghosh, A. Majumdar and A. Pal, *Mater. Res. Bull.*, 2021, **133**, 111074.

4 S. Li, B. Xue, J. Chen, Y. Liu, J. Zhang, H. Wang and J. Liu, *Sep. Purif. Technol.*, 2021, **254**, 117579.

5 M. Gaballah, J. Guo, H. Sun, D. Aboagye, M. Sobhi, A. Muhmood and R. Dong, *Bioresour. Technol.*, 2021, **333**, 125069.

6 C. Hou, H. Liu and F. Mohammad, *J. Solid State Chem.*, 2021, **300**, 122288.

7 Y. Sun, L. Wang, T. Wang, X. Liu, T. Xu, M. Wei, L. Yang and C. Li, *J. Alloys Compd.*, 2021, **862**, 156963.

8 G. Yang, Y. Zhu, Y. Liang, J. Yang, K. Wang, Z. Zeng, R. Xu and X. Xie, *Appl. Surf. Sci.*, 2021, **539**, 148038.

9 C. Hou, H. Liu and M. Bakhtari, *Mater. Sci. Semicond. Process.*, 2021, **136**, 106142.

10 A. Huang, M. Yan, J. Lin, L. Xu, H. Gong and H. Gong, *Int. J. Environ. Res. Public Health*, 2021, **18**, 4909.

11 W. Zhong, B. Xiao, Z. Lin, Z. Wang, L. Huang, S. Shen, Q. Zhang and L. Gu, *Adv. Mater.*, 2021, **33**, 2007894.

12 Z. Song, Y. Ma, C. Li, M. Xu and C. Zhang, *Adv. Mater. Sci. Eng.*, 2019, **2019**, 3532576.

13 S. Shurbaji, P. Huong and T. Altahtamouni, *Catalysts*, 2021, **11**, 437.

14 V. Hasija, V. Nguyen, A. Kumar, P. Raizada, V. Krishnan, A. Khan, P. Singh, E. Lichtfouse, C. Wang and P. Huong, *J. Hazard. Mater.*, 2021, **413**, 125324.

15 Z. Lin, B. Xiao, Z. Wang, W. Tao, S. Shen, L. Huang, J. Zhang, F. Meng, Q. Zhang, L. Gu and W. Zhong, *Adv. Func. Mater.*, 2020, **59**, 22743–22748.

16 S. Lai, J. Park, S. Yoo, J. Ha, E. Song and S. Cho, *Int. J. Hydrogen Energy*, 2016, **41**, 3428–3435.

17 M. Ota, Y. Hirota, Y. Uchida, Y. Sakamoto and N. Nishiyama, *Langmuir*, 2018, **34**, 6814–6819.

18 Y. Zhang, M. Kuang, X. Hao, Y. Liu, M. Huang, X. Guo, J. Yan, G. Han and J. Li, *J. Power Sources*, 2014, **270**, 675–683.

19 J. Lyu, L. Zhou, J. Shao, Z. Zhou, J. Gao, J. Li, Y. Dong and Z. Wang, *Chem. Eng. J.*, 2020, **400**, 125927.

20 M. Du, G. Zeng, J. Huang, D. Sun, Q. Li, G. Wang and X. Li, *ACS Sustainable Chem. Eng.*, 2019, **7**, 9717–9726.

21 M. Hinojosa-Reyes, R. Camposeco-Solis and F. Ruiz, *Microporous Mesoporous Mater.*, 2019, **276**, 183–191.

22 W. Zhong, Z. Wang, N. Gao, L. Huang, Z. Lin, Y. Liu, F. Meng, J. Deng, S. Jin, Q. Zhang and L. Gu, *Angew. Chem., Int. Ed.*, 2020, **59**, 22743–22748.

23 W. Soontornchaiyakul, T. Fujimura, H. Usami and R. Sasai, *RSC Adv.*, 2017, **7**, 21790–21795.

24 Y. Jian, H. Liu, J. Zhu, Y. Zeng, Z. Liu, C. Hou and S. Pu, *RSC Adv.*, 2020, **10**, 42860–42873.

25 J. Pan, Z. Dong, B. Wang, Z. Jiang, C. Zhao, J. Wang, C. Song, Y. Zheng and C. Li, *Appl. Catal. B-Environ.*, 2019, **242**, 92–99.

26 G. Zhang, G. Kim and W. Choi, *Energy Environ. Sci.*, 2014, **7**, 954–966.

27 S. Wu, H. Hu, Y. Lin, J. Zhang and Y. Hu, *Chem. Eng. J.*, 2020, **382**, 122842.

28 Y. Chang, J. Lin and C. Chou, *J. Photochem. Photobiol., A*, 2020, **400**, 112666.

29 M. Xiao, D. Shen, K. Musselman, W. Duley and Y. Zhou, *Nanoscale*, 2018, **10**, 6069–6079.

30 J. Tan, S. Gavrielides, H. Xu, W. Thompson and M. Maroto-Valer, *RSC Adv.*, 2020, **10**, 27989–27994.

31 Y. Zhang, T. Xia, M. Shang, P. Wallenmeyer, D. Katelyn, A. Peterson, J. Murowchick, L. Dong and X. Chen, *RSC Adv.*, 2014, **4**, 16146–16152.

32 Y. Zhang, M. Shang, Y. Mi, T. Xia, P. Wallenmeyer, J. Murowchick, L. Dong, Q. Zhang and X. Chen, *ChemPlusChem*, 2014, **79**, 1159–1166.

33 C. Zhang, L. Tian, L. Chen, X. Li, K. Lv and K. Deng, *Chin. J. Catal.*, 2018, **39**, 1373–1383.

34 M. Kowalkinska, S. Dudziak, J. Karczewski, J. Ryl, G. Trykowski and A. Zielinska-Jurek, *Chem. Eng. J.*, 2021, **404**, 126493.

35 L. Chen, C. Zhang, L. Wu, K. Lv, K. Deng and T. Wu, *Nanoscale Res. Lett.*, 2018, **13**, 336.

36 S. Ma, J. Deng, Y. Xu, W. Tao, X. Wang, Z. Lin, Q. Zhang, L. Gu and W. Zhong, *J. Energy Chem.*, 2022, **66**, 560–565.

37 C. Hou, J. Xie, H. Yang, S. Chen and H. Liu, *RSC Adv.*, 2019, **9**, 37911–37918.

38 R. Zhang, C. Wang, H. Chen, H. Zhao, J. Liu, Y. Li and B. Su, *Acta Phys.-Chim. Sin.*, 2020, **36**, 1803014.

39 B. Fang, A. Bonakdarpour, K. Reilly, Y. Xing, F. Taghipour and D. Wilkinson, *ACS Appl. Mater. Interfaces*, 2014, **6**, 15488–15498.

40 B. Fang, Y. Xing, A. Bonakdarpour, S. Zhang and D. Wilkinson, *ACS Sustainable Chem. Eng.*, 2015, **3**, 2381–2388.

41 Y. Liu, S. Shen, Z. Li, D. Ma, G. Xu and B. Fang, *Mater. Charact.*, 2021, **174**, 111031.

42 Z. Wang, B. Xiao, Z. Lin, Y. Xu, Y. Lin, F. Meng, Q. Zhang, L. Gu, B. Fang, S. Guo and W. Zhong, *Angew. Chem., Int. Ed.*, 2021, **60**, 23388–23393.

43 G. Liao, F. He, Q. Li, L. Zhong, R. Zhao, H. Che, H. Gao and B. Fang, *Prog. Mater. Sci.*, 2020, **112**, 100666.

44 Y. Zhang, X. Wang, F. Luo, Y. Tan, L. Zeng, B. Fang and A. Liu, *Appl. Catal. B-Environ.*, 2019, **256**, 117852.

45 G. Liao, J. Fang, Q. Li, S. Li, Z. Xu and B. Fang, *Nanoscale*, 2019, **11**, 7062–7096.

46 B. Fang, S. Fan, J. Kim, M. Kim, M. Kim, N. Chaudhari, J. Ko and J. Yu, *Langmuir*, 2010, **26**, 11238–11243.

47 Y. Xing, B. Fang, A. Bonakdarpour, S. Zhang and D. Wilkinson, *Int. J. Hydrogen Energy*, 2014, **39**, 7859–7867.

48 B. Fang, M. Kim, J. Kim and J. Yu, *Langmuir*, 2008, **24**, 12068–12072.

49 Z. Ul Abideen and F. Teng, *CrystEngComm*, 2018, **20**, 7866–7879.

50 S. Wu, H. Hu, Y. Lin, J. Zhang and Y. Hu, *Chem. Eng. J.*, 2020, **382**, 122842.

51 E. Abdelsalam, Y. Mohamed, S. Abdelkhalik, H. ElNazer and Y. Attia, *Environ. Sci. Pollut. Res.*, 2020, **27**, 35828–35836.

52 W. Zhang, J. Zhu, J. He, L. Xu and L. Hu, *Environ. Sci. Pollut. Res.*, 2020, **126**, 630.

53 Y. Bai, P. Yang, L. Wang, B. Yang, H. Xie, Y. Zhou and L. Ye, Ultrathin $Bi_4O_5Br_2$ nanosheets for selective photocatalytic CO_2 conversion into CO, *Chem. Eng. J.*, 2019, **360**, 473–482.

54 C. Chen, W. Ma and J. Zhao, *Chem. Soc. Rev.*, 2010, **39**, 4206–4219.

55 S. Chen, J. Du, L. Shen and W. Chen, *J. Phys. Chem. Solids*, 2021, **149**, 109784.

56 E. Doluel, U. Kartal, T. Dikici and M. Yurddaskal, *J. Electron. Mater.*, 2020, **49**, 3849–3859.

57 Y. Zheng, X. Hu and P. Yang, *Crystengcomm*, 2018, **20**, 4485–4491.

58 C. Zhao, J. Guo, C. Yu, Z. Zhang, Z. Sun and X. Piao, *Mater. Chem. Phys.*, 2020, **248**, 122873.

59 C. Hou, H. Liu and Y. Li, *RSC Adv.*, 2021, **11**, 14957–14969.

60 Z. Liu, X. Liu, Q. Lu, Q. Wang and Z. Ma, *J. Taiwan Inst. Chem. Eng.*, 2019, **96**, 214–222.

61 S. Zhang, Z. Yin, L. Xie, J. Yi, W. Tang, T. Tang, J. Chen and S. Cao, *Ceram. Int.*, 2020, **46**, 8949–8957.

62 Y. Xiao, Z. Peng, S. Zhang, Y. Jiang, X. Jing, X. Yang, J. Zhang and L. Ni, *J. Mater. Sci.*, 2019, **54**, 9573–9590.

63 Z. Wang, B. Xiao, Z. Lin, Y. Xu, Y. Lin, F. Meng, Q. Zhang, L. Gu, B. Fang, S. Guo and W. Zhong, *J. Energy Chem.*, 2021, **60**, 23388–23393.

64 D. Cao, H. An, X. Yan, Y. Zhao, G. Yang and H. Mei, *Acta Phys.-Chim. Sin.*, 2020, **36**, 1901051.

65 Z. M. Liu, G. Liu and X. Hong, *Acta Phys.-Chim. Sin.*, 2019, **35**, 215–222.

66 Y. Jiang, Z. Peng, S. Zhang, F. Li, Z. Liu, J. Zhang, Y. Liu and K. Wang, *Ceram. Int.*, 2018, **44**, 6115–6126.